




RESEARCH ARTICLE | MARCH 21 2024

Phase-field modeling of ATG instability in Allen–Cahn framework

Xuyang Chen   ; Guangchao Li  ; Feng Lin

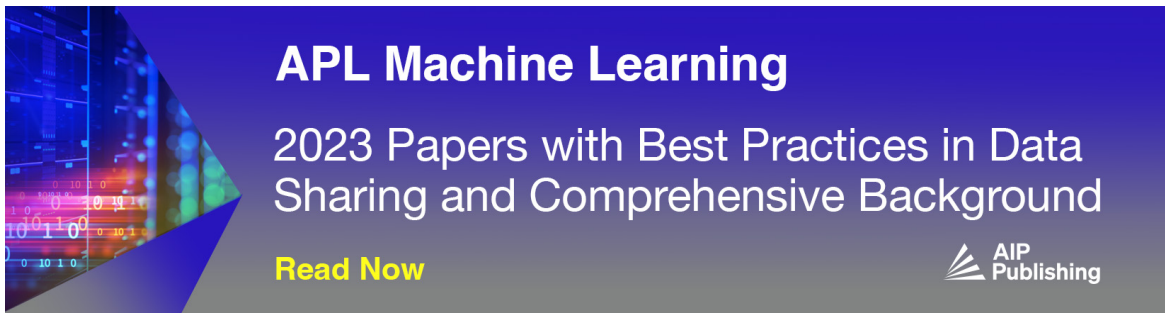


AIP Advances 14, 035044 (2024)


<https://doi.org/10.1063/5.0190761>



17 April 2024 10:44:32



APL Machine Learning
2023 Papers with Best Practices in Data Sharing and Comprehensive Background
[Read Now](#)



Phase-field modeling of ATG instability in Allen–Cahn framework

Cite as: AIP Advances 14, 035044 (2024); doi: 10.1063/5.0190761

Submitted: 8 December 2023 • Accepted: 1 March 2024 •

Published Online: 21 March 2024



Xuyang Chen,^{1,2,a)}  Guangchao Li,^{2,b)}  and Feng Lin^{1,c)}

AFFILIATIONS

¹ Department of Mechanical Engineering, Tsinghua University, Beijing 100084, China

² Institute of Applied Materials-Microstructure Modelling and Simulation, Karlsruhe Institute of Technology, Straße am Forum 7, 76131 Karlsruhe, Germany

^{a)} Author to whom correspondence should be addressed: chenxy.2018@tsinghua.org.cn

^{b)} Also at: Institute of Nuclear and New Energy Technology, Key Laboratory of Advanced Reactor Engineering and Safety of Ministry Education, Tsinghua University, Beijing 100084, China.

^{c)} Also at: Biomanufacturing and Rapid Forming Technology Key Laboratory of Beijing, Tsinghua University, Beijing 100084, China. Electronic address: linfeng@tsinghua.edu.cn

ABSTRACT

The phenomenon of Asaro–Tiller–Grinfeld (ATG) instability is common in the molecular beam epitaxy (MBE) process. In order to investigate the ATG instability, a two-dimensional mathematical model is established, which considers elastic stress. The phase-field method is utilized to simulate the interface evolution and the stress distribution. Furthermore, the Allen–Cahn approach, coupled with the motion of the interface, is used to investigate the morphology evolution. The results show that the thin film becomes unstable when it reaches a critical value. The critical thickness of the thin film is about 5.08 nm. The interface breaks into several parts due to the effect of elastic stress. The validity and correctness of the model are verified by the relevant theoretical results. Moreover, the numerical model can provide the basis for optimizing the ATG instability phenomenon in the MBE process.

© 2024 Author(s). All article content, except where otherwise noted, is licensed under a Creative Commons Attribution (CC BY) license (<http://creativecommons.org/licenses/by/4.0/>). <https://doi.org/10.1063/5.0190761>

I. INTRODUCTION

In the fabrication of nanostructures and diodes, molecular beam epitaxy (MBE) plays a critical role.¹ MBE involves vaporizing the source material and conscientiously depositing it onto a substrate in the form of a “beam”. Even though MBE allows precise control over the chemical composition of the processed material, elastic instability is often associated with it.² This instability is referred to as Asaro–Tiller–Grinfeld (ATG) instability.³

The difference in the lattice parameters of the source material and substrate, along with the disparity in the temperature, introduces non-hydrostatic loading as a misfit strain and thermal expansion. A relaxation of this strain induces morphological changes, which alter the configuration of the interface. Accordingly, ATG instability is characteristically associated with the morphological evolution of the interface under the combined influence of

surface and elastic energy, which is introduced by non-hydrostatic loading.⁴ Owing to its noticeable effect on the processing of multilayered semiconductors, ATG instability is extensively analyzed.⁵ In addition to experimental techniques, theoretical treatments have been adopted to understand the interplay of surface and elastic energy in governing the configuration of the interface. The phase field method is a mathematical tool for describing interfaces and their motion. Recently, the morphological evolution of the interface associated with ATG instability has been modeled in a phase-field framework.^{6–8}

Kassner *et al.*⁹ developed a phase-field approach describing the dynamics of a strained solid in contact with its melt. They showed that their phase-field approach recovered the sharp interface limit corresponding to the continuum model equations describing the Asaro–Tiller–Grinfeld instability.

Huang and Desai¹⁰ investigated the stress-driven morphological instability of epitaxially growing multilayer films, which are

coherent and dislocation-free. They constructed a direct elastic analysis, from which we derive the elastic state of the system recursively in terms of that of the old states of the buried layers.

Yeon *et al.*¹¹ presented a phase-field model for the surface corrugation of elastically stressed films, where surface diffusion is a dominant mass transport mechanism. They performed matched asymptotic expansion analysis and demonstrated that the phase-field model reduces to the previously existing sharp interface model of the Asaro–Tiller–Grinfeld instability in the sharp interface limit.

Using a phase-field model, Chirranjeevi *et al.*¹² studied the microstructural evolution of multiple layers of elastically stiff films embedded in an elastically soft matrix. In view of the mismatch of elastic modulus and volume fraction, they drew a stability diagram for the most probable form of breakup. They rationalized their results in terms of the initial driving force for destabilization and supported their conclusions by simulations in elastically anisotropic systems.

Zaeem *et al.*¹³ used the Galerkin finite element formulation for coupled Cahn–Hilliard elasticity problem maps of different evolution paths to develop the model in the parameter space of the relative thicknesses of the initial phases. They considered the relative importance of the elastic and chemical energy of the system and developed maps for different cases.

Köhler *et al.*¹⁴ demonstrated that curvature-induced stress in surface crystals can be relaxed by the long-wavelength ATG instability with a combined numerical and analytical approach.

Zhang and Tang¹⁵ presented a linear stability analysis to demonstrate that a flat coherent phase boundary, formed by the intercalation of solutes into a compound, is unstable against perturbations with wavelengths larger than a critical wavelength. They found that uniform intercalation cannot be achieved unless the phase boundary moves at a speed greater than the critical velocity.

Despite several advancements, this instability in the phase-field approach is always modeled by treating the order parameter as a conserved variable and, consequently, solving its temporal evolution in the Cahn–Hilliard framework. This treatment is not only numerically tedious but also computationally intensive. Alternatively, ATG instability can efficiently be modeled by solving the evolution of the order parameter in the Allen–Cahn framework, by separately imposing the necessary constraints.^{16–18} Correspondingly, the proposed work aims to develop a computationally efficient approach for the phase-field modeling of morphological changes accompanying ATG instability.

In this publication, we investigate ATG instability in Allen–Cahn frameworks. The model involves coupling the elastic energy density with the redistribution energy.¹⁹ The techniques treat the order parameter as a non-conserved variable and adopts the Allen–Cahn framework.²⁰ The jump condition elasticity is considered to investigate how the elastic mechanics affect the evolution. The morphology and stress at different times are calculated and analyzed. In addition, the thin film is strongly influenced by surface and interface effects, and the evolution at different G_{ab} values is compared and analyzed. By examining the simulation techniques and computational efficiency, the experimental equation of the critical thickness is introduced. Then, we compare the simulation results with the empirical formula to verify the validity of the model.

II. NUMERICAL MODEL

A. Asaro–Tiller–Grinfeld instability

When the elastic energy builds up, solids can release this energy in different ways. One is by plastic deformation, involving dislocations, and another is by elastic deformation, which is commonly seen in thin-film growth.

A non-hydrostatically strained solid is in contact with its elastic energy due to the morphological instability at the interface. An accidental corrugation of the surface causes the stress to decrease at its tip and increase in the valleys. The solid can decrease its average elastic energy density by growing tips and increasing the depths of valleys, which was first predicted by Asaro and Tiller. Ever since the independent rediscovery of the instability by Grinfeld and Srolovitz, it has often been referred to as the Asaro–Tiller–Grinfeld (ATG) instability.²¹ Figure 1 shows how the strained film [due to the lattice parameter of the substrate (red) being imposed on the film (blue)] can relieve the stresses at the tips. However, the stress concentration at the troughs increases. Hence, once the undulation starts, it continues to grow.²²

In this section, we introduce the behavior of the ATG instability in brief for the case where the bulk is transported predominantly by surface diffusion, which has been introduced several times by other researchers. From now on, the behavior of a solid subjected to uniaxial stress at the surface is described, where the material transport is carried out by surface diffusion. For simplicity, we restrict ourselves to planar strain and isotropic elastic properties of the solid. For a two-phase system, the potential at the interface is given by⁷

$$\mu^s(x) = \mu_0 + \gamma\kappa_c(x) + \frac{1-\nu^2}{2E}(\sigma_{tt} - \sigma_{nn})^2. \quad (1)$$

In Eq. (1), the effect of gravity is ignored. γ is the surface free energy, κ_c is the local curvature of the interface, μ_0 denotes the chemical free energy of the reference state (here, μ_0 can be set to zero), E and ν represent Young's modulus and Poisson's ratio of the solid phase, respectively, and σ_{tt} and σ_{nn} are the purely tangential and normal components of the stress tensor at the interface, respectively.

If the mass is transported by surface diffusion only, the mass flux \vec{J}_s along the interface is proportional to the surface gradient of the chemical potential at the interface, and the total amount of

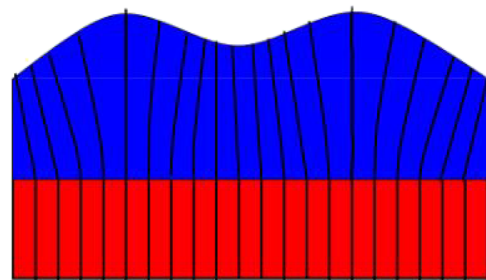


FIG. 1. Illustration of the Asaro–Tiller–Grinfeld (ATG) instability principle.

material should be conserved.⁶ The equation of the interface motion is as follows:

$$v_n = -\frac{\partial}{\partial s} \vec{J}_s = \frac{\partial}{\partial s} \left[M_s \frac{\partial}{\partial s} \left(\mu_0 + \gamma \kappa_c + \frac{1-\nu^2}{2E} (\sigma_{tt} - \sigma_{nn})^2 \right) \right], \quad (2)$$

where M_s represents the atomic mobility along the interface and $\frac{\partial}{\partial s}$ denotes the surface gradient, which ensures that the diffusion occurs only along the surface.

If M_s is constant, the change in the interface position $h(x)$ in time is⁹

$$\frac{\partial h}{\partial t} = M_s \frac{1}{\sqrt{1+h_x^2}} \frac{\partial^2 \mu^s}{\partial s^2}, \quad (3)$$

where h_x represents $\frac{\partial h}{\partial x}$. This equation describes how the interface position $h(x)$ of a stressed solid changes over time. M_s is a mobility constant, h_x is the spatial derivative of the interface height (representing the slope of the interface), and $\frac{\partial^2 \mu^s}{\partial s^2}$ is the second spatial derivative of the chemical potential along the interface. The equation essentially links the temporal evolution of the interface height to its curvature and the chemical potential gradient, under the influence of stress.

The linear stability of the planar surface bounding the stressed solid can now be analyzed by considering perturbations on the surface.²³ Substituting an initial sinusoidal perturbation, $h_0 \sin(qx)$, we obtain the following dispersion relation, where ω is the growth rate of the surface perturbation, q is the wave number, and σ_0 is the uniaxial stress:

$$\omega = M_s \left(\frac{2(1-\nu^2)}{E} \sigma_0^2 q^3 - \gamma q^4 \right). \quad (4)$$

This dispersion relation gives the growth rate (ω) of the surface perturbation as a function of the wave number q . Here, σ_0 is the uniaxial stress, ν is Poisson's ratio, E is Young's modulus of the material, and γ is the surface energy. The equation indicates how different modes of surface perturbations grow or decay over time, depending on these material properties and the applied stress. Thus, there is a set of unstable modes where the wave number $q < q_c$,

$$q_c = \frac{2\sigma_0^2(1-\nu^2)}{E\gamma}, \quad (5)$$

with the most unstable mode at $q = q_m = 0.75q_c$. This equation defines the critical wave number q_c . For wave numbers less than q_c , the perturbations on the surface are unstable and will grow over time. This critical wave number is dependent on the material's mechanical properties and the applied stress. These results imply that the surface diffusion smoothed the perturbations of wavelengths, which are smaller than $\lambda_c (= \frac{2\pi}{q_c})$, while long wavelength perturbations grow unstably.

B. Phase-field model

Based on a free energy functional of Ginzburg–Landau type, a multicomponent multiphase-field model is employed to simulate the isothermal chemo-mechanical transformation process.²⁴ We outline our phase field model for systems that are elastically inhomogeneous

and anisotropic.²⁵ The model is based on the Allen–Cahn equation. Our phase field formulation starts with the following expression for the total free energy F of a system. The functional is expressed as

$$F(\phi, \nabla\phi, \epsilon) = F_{intf}(\phi, \nabla\phi) + F_{el}(\phi, \epsilon) = \int_V f_{intf} + f_{el} dV, \quad (6)$$

where f_{el} denotes the elastic energy density contribution as a function of the local strain ϵ . As for the two-phase system, F_{intf} can be expressed as

$$F_{intf}(\phi, \nabla\phi) = \int_V f_{grad} + f_{pot} dV = \int_V \epsilon a(\phi, \nabla\phi) + \frac{1}{\epsilon} \omega_{ob}(\phi) dV, \quad (7)$$

where ϵ is a length parameter, which governs the width of the diffuse interface. The gradient energy density is expressed by the surface energy density $\gamma_{\alpha\beta}$ and the normal vector to the $\alpha - \beta$ interface,²⁴

$$a(\nabla\phi) = \gamma_{\alpha\beta} |\nabla\phi|^2. \quad (8)$$

The generalized gradient vector can be expressed as

$$q_{\alpha\beta} = \phi_\alpha \nabla\phi_\beta - \phi_\beta \nabla\phi_\alpha. \quad (9)$$

Then Eq. (8) yields

$$a(\nabla\phi) = \gamma_{\alpha\beta} (q_{\alpha\beta})^2. \quad (10)$$

As for most of the phase-field models, the potential energy density can be expressed as²⁴

$$\omega_{ob} = \frac{16}{\pi^2} \gamma_{\alpha\beta} \phi(1-\phi). \quad (11)$$

The elastic energy density is defined as follows:²⁶

$$F_{el}(\phi, \epsilon) = \int_V f_{el}(\phi, \epsilon) dV = \int_V \sum_\alpha f_{el}^\alpha h^\alpha(\phi) dV, \quad (12)$$

where $h(\phi) = \phi$ or $h(\phi) = \phi^2(3-2\phi)$. The normalized interpolation function²⁷ can be expressed as

$$h^\alpha(\phi) = \frac{h(\phi_\alpha)}{\sum_\beta h(\phi_\beta)}. \quad (13)$$

The elastic strain energy of phase α is

$$f_{el}^\alpha(\epsilon_{el}^\alpha) = \frac{1}{2} \epsilon_{el}^\alpha \cdot \sigma^\alpha(\epsilon_{el}^\alpha). \quad (14)$$

According to Hooke's Law, the phase inherent stresses can be calculated as $\sigma^\alpha(\epsilon_{el}^\alpha) = \mathbf{C}^\alpha[\epsilon_{el}^\alpha]$, where \mathbf{C}^α is the stiffness tensor of phase α in the Voigt notation.¹⁶ According to the published literature,²⁸ the elastic strain energy of phase α yields

$$f_{el}^\alpha(\epsilon_{el}^\alpha) = \frac{1}{2} \epsilon_{el}^\alpha \cdot \mathbf{C}^\alpha[\epsilon_{el}^\alpha]. \quad (15)$$

The evolution of order parameters can be computed via a variational approach as the summation of dual interactions,²⁹

$$\frac{\partial\phi_\alpha}{\partial t} = -\frac{1}{\epsilon N} \sum_{\beta \neq \alpha}^N M_{\alpha\beta} \left(\frac{\delta F}{\delta\phi_\alpha} - \frac{\delta F}{\delta\phi_\beta} \right), \quad (16)$$

where $\tilde{N} \leq N$ is the number of active phases and $M_{\alpha\beta}$ denotes the mobility of an $\alpha - \beta$ interface.

The variational derivative of the overall free energy with respect to ϕ_α reads²⁶

$$\frac{\delta f}{\delta \phi_\alpha} = \left(\frac{\partial}{\partial \phi_\alpha} - \nabla \cdot \frac{\partial}{\partial \nabla \phi_\alpha} \right) f(\phi, \nabla \phi, \varepsilon). \quad (17)$$

As we focus on the mechanical contributions of the total energy functional, the derivative $\frac{\delta f_{el}}{\delta \phi}$ is given below.

C. Numerical scheme for elastic field calculation

In the phase-field model, the calculation of the elastic field is crucial for accurately capturing the mechanical behavior of the system under study. The elastic field is derived from the local strain tensor and the corresponding stress tensor, which are functions of the displacement field. In this research, the numerical implementation for studying ATG instability in a phase-field model using finite difference methods can be detailed as follows:

The simulation domain is discretized into uniform grids, with dimensions $\Delta x = \Delta y = \Delta z = 0.5$. In this study, the interface width is fixed by the length parameter $\varepsilon = 3 \times \Delta x$, which corresponds to 8 grid points at the interface. This setting is critical for capturing the interface dynamics accurately. This discretization allows for the calculation of spatial derivatives needed to compute strain and stress tensors.

The strain tensor ε is calculated from the displacement field \mathbf{u} using the following relation:

$$\varepsilon = \frac{1}{2} (\nabla \mathbf{u} + (\nabla \mathbf{u})^T). \quad (18)$$

The displacement field is obtained from the phase field variables and evolves according to the mechanical equilibrium condition.

The stress tensor σ is computed using Hooke's law for isotropic materials,

$$\sigma = \lambda \operatorname{tr}(\varepsilon) \mathbf{I} + 2\mu \varepsilon, \quad (19)$$

where λ and μ are Lamé's first and second parameters, respectively, derived from Young's modulus and Poisson's ratio.

The computation of the elastic field is implemented using the following steps: 1. Initialization of the Displacement Field: Initialize the displacement field \mathbf{u} based on the boundary conditions and initial conditions of the simulation. 2. Strain Tensor Calculation: For each grid point, calculate the strain tensor ε using the spatial derivatives of the displacement field. 3. Stress Tensor Calculation: Compute the stress tensor σ at each grid point using the strain tensor and the material's elastic constants. 4. Mechanical Equilibrium: Solve the mechanical equilibrium equation $\nabla \cdot \sigma = 0$ using an appropriate numerical method (e.g., finite difference method and finite element method). 5. Iterative Solution: Iteratively solve for the displacement field until mechanical equilibrium is reached throughout the domain. 6. Feedback to the Phase Field Model: The computed stress tensor is then fed back into the phase field model to simulate the evolution of the system under mechanical stress. This numerical scheme enables the accurate calculation of the elastic field, which is essential for modeling the ATG instability and understanding the mechanical response of the material system under study.

The iterative solution ensures that the system reaches mechanical equilibrium, aligning with the physical behavior of the material.

D. Jump condition elasticity

In this work, the model fulfills mechanical jump conditions, the static impulse balance, and Hadamard's compatibility condition.

The mechanical jump conditions for a bounded solid-solid transition are the underlying physical equations of the proposed model. The force balance reads³⁰

$$(\sigma^\alpha - \sigma^\beta) \mathbf{n} = \sigma \mathbf{n} = \mathbf{0}. \quad (20)$$

It implies that the corresponding jump of stresses σ in the normal vector \mathbf{n} at the interface between α and β phase is zero. The kinematic compatibility condition,³⁰ known as Hadamard jump condition,

$$\mathbf{H} = \mathbf{a} \otimes \mathbf{n}, \quad (21)$$

represents a no-slip condition in the tangential directions of the singular planes in solids, in which $\mathbf{a} \otimes \mathbf{n}$ is the dyadic product of an arbitrary vector, \mathbf{a} , and the normal vector and \mathbf{H} denotes the jump of the displacement gradient \mathbf{H} . Apart from the continuity of the displacement field \mathbf{u} , the Hadamard jump condition follows³⁰

$$\nabla \mathbf{u} = \mathbf{a} \otimes \mathbf{n}^T. \quad (22)$$

$(\mathbf{a} \mathbf{n}^T)_{ij} = a_i n_j$ is the dyadic product of an arbitrary vector \mathbf{a} and the normal vector \mathbf{n} . The jump of the deformation gradient $\nabla \mathbf{u}$ vanishes in the tangential direction and implies a no slip boundary condition. If we multiply two tangential vectors \mathbf{t} and \mathbf{s} with $\langle \mathbf{t}, \mathbf{n} \rangle = t_i n_i = 0$ and $\langle \mathbf{s}, \mathbf{n} \rangle = 0$, it can be seen that $\nabla \mathbf{u} \mathbf{t} = 0$ and $\nabla \mathbf{u} \mathbf{s} = 0$.

The momentum balance equation can be solved as follows:

$$\nabla \cdot \sigma = 0. \quad (23)$$

The evolution of displacement field u is calculated until the mechanical equilibrium $\rho \ddot{u} = 0$ is reached. $\nabla \cdot \sigma$ defines the stress divergence. In this case, the evolution displacement field \mathbf{u} is given by the static balance of momentum,

$$\nabla \cdot \bar{\sigma}(\phi, \sigma^\alpha) = 0. \quad (24)$$

The volume-averaged stress can be expressed as

$$\bar{\sigma}(\phi, \sigma^\alpha) = \sum_\alpha \sigma^\alpha h^\alpha(\phi). \quad (25)$$

As for ϕ_α , there are some assumptions: the effect of the gradient field and the mechanical microstresses are not examined in more detail. Under these assumptions, the derivative of f_{el} is given in Ref. 28.

E. Non-dimensionalization of equations

In order to facilitate the analysis and numerical implementation of the model, it is beneficial to non-dimensionalize the equations governing the Asaro–Tiller–Grinfeld (ATG) instability and the phase-field model. Non-dimensionalization helps in reducing the complexity of the problem, understanding the relative importance of different terms, and simplifying the comparison between different cases.³¹ We will use characteristic scales of length, energy, and time to transform the equations into their dimensionless form.

1. Characteristic scales

1. Length Scale (L): The characteristic length scale is chosen as the average thickness of the thin film or the wavelength of the perturbation.
2. Energy Scale (E): The characteristic energy scale is set by the surface free energy, γ .
3. Time Scale (T): The characteristic time scale is chosen based on the atomic mobility, M_s , and the length scale.

2. Non-dimensional parameters

In this theoretical study, time (t) is not dimensionalized. This approach allows for a direct interpretation of the simulation results in terms of real-time scales, which is crucial for comparing with experimental data or other theoretical models. Using the above-mentioned scales, we define the following non-dimensional parameters: Non-dimensional length: $\tilde{x} = \frac{x}{L}$; non-dimensional energy: $\tilde{E} = \frac{E}{\gamma}$; non-dimensional time: $\tilde{t} = \frac{t}{T}$.

3. Transformation of equations

Using these non-dimensional parameters, we transform the key equations of the model:

1. Chemical Potential:

$$\tilde{\mu}^s(\tilde{x}) = \tilde{\mu}_0 + \kappa_c(\tilde{x}) + \frac{1 - \nu^2}{2\tilde{E}}(\sigma_{tt} - \sigma_{nn})^2. \quad (26)$$

2. Interface Motion:

$$\tilde{v}_n = -\frac{\partial}{\partial \tilde{s}} \tilde{J}_s = \frac{\partial}{\partial \tilde{s}} \left(\tilde{M}_s \frac{\partial \tilde{\mu}^s}{\partial \tilde{s}} \right). \quad (27)$$

3. Interface Position:

$$\frac{\partial \tilde{h}}{\partial \tilde{t}} = \tilde{M}_s \frac{1}{\sqrt{1 + (\partial \tilde{h} / \partial \tilde{x})^2}} \frac{\partial^2 \tilde{\mu}^s}{\partial \tilde{s}^2}. \quad (28)$$

4. Dispersion Relation:

$$\tilde{\omega} = \tilde{M}_s \left(\frac{2(1 - \nu^2)}{\tilde{E}} \tilde{\sigma}_0^2 \tilde{q}^3 - \tilde{q}^4 \right), \quad (29)$$

$$\frac{\partial f_{el}(\phi, f_{el}^\alpha)}{\partial \phi_\alpha} = \left[f_{el}^\alpha - \frac{\partial f_{el}^\alpha}{\partial \epsilon_n^\alpha} \cdot \epsilon_n^\alpha - \left(f_{el}^\beta - \frac{\partial f_{el}^\beta}{\partial \epsilon_n^\beta} \cdot \epsilon_n^\beta \right) \right] \frac{\partial h^\alpha}{\partial \phi_\alpha}. \quad (30)$$

F. Material properties

The material properties of InAs³² are shown in Table I.³³ The values of C11, C12, and C44 are 118, 52.8, and 32.6, respectively.³⁴

To discuss the Asaro–Tiller–Grinfeld (ATG) instability, the terms “Lambda” and “Mu” in Table I are typically used to represent the Lamé constants in the context of elasticity and mechanical properties of materials, respectively. The Lamé constants, usually denoted as λ and μ , are parameters that describe the mechanical response of isotropic materials. They are related to the more commonly known

TABLE I. The material properties of InAs.

Item	Quantity
Young’s modulus (GPa)	51.4
Poisson’s ratio	0.36
Shear modulus (GPa)	18.5
Thermal expansion coefficient ($10^{-6}/K$)	4.6
Lattice constant (Å)	6.05
Eigenstrain	0.0373
Lambda	48.59
Mu	18.9

material properties, Young’s modulus (E), and Poisson’s ratio (ν) and are key in defining the material’s response to stress and strain.³⁵

The relationships between these constants are given by

$$\lambda = \frac{E\nu}{(1 + \nu)(1 - 2\nu)},$$

$$\mu = \frac{E}{2(1 + \nu)}.$$

For the material properties of InAs, given a Young’s modulus (E) of 51.4 GPa and Poisson’s ratio (ν) of 0.36, we can calculate the corresponding Lamé constants λ and μ as ≈ 48.59 GPa and ≈ 18.90 GPa, respectively.

To include a stability diagram for the system presented in Table I of the article, we need to consider the key parameters and relationships that influence the stability of the Asaro–Tiller–Grinfeld (ATG) instability in the context of our phase-field model. Based on the equations and material properties provided, a stability diagram can be constructed to illustrate the relationship between the critical wave number (q_c), the surface energy (γ), and other material parameters such as Young’s modulus (E), Poisson’s ratio (ν), and the uniaxial stress (σ_0).

The critical wave number (q_c) for instability, given by

$$q_c = \frac{2\sigma_0^2(1 - \nu^2)}{E\gamma},$$

is a crucial parameter in determining the stability of the system. The stability diagram can be plotted with q_c on one axis (indicating the onset of instability) and a combination of material parameters and surface energy on the other axis.

We create a diagram with q_c on the y-axis and γ (surface energy) on the x-axis for different values of uniaxial stress (σ_0), as shown in Fig. 2. This diagram will illustrate how the stability threshold changes with varying surface energies and stresses.

To proceed with creating this diagram, We calculate and plot the stability diagram based on the provided formula and a range of γ and σ_0 values. We set a range for γ and σ_0 based on typical values for materials such as InAs. We will use Young’s modulus (E) and Poisson’s ratio (ν) from Table I.

The stability diagram for the Asaro–Tiller–Grinfeld (ATG) instability is illustrated in Fig. (2). In this diagram, the critical wave

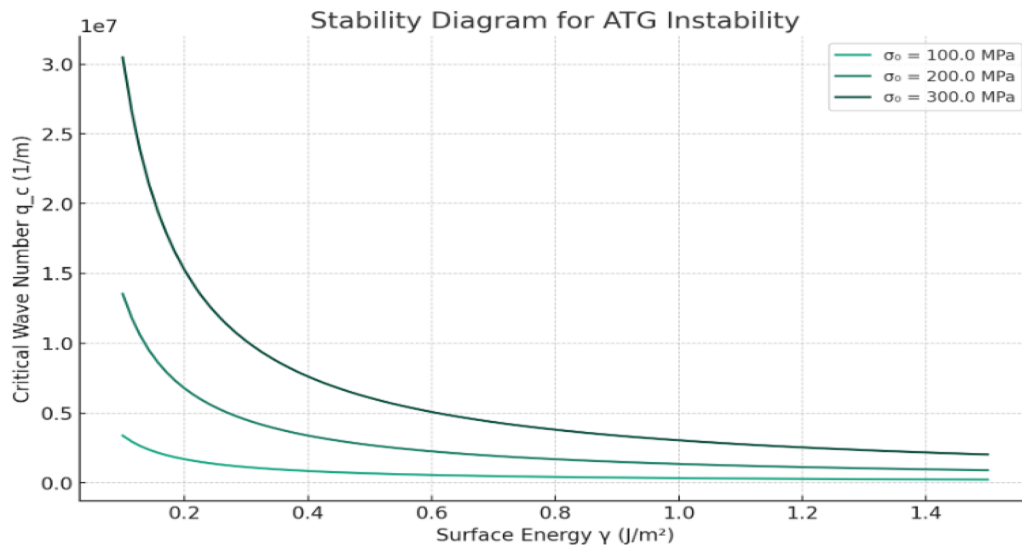


FIG. 2. Stability diagram for the Asaro–Tiller–Grinfeld (ATG) instability.

number q_c is plotted against the surface energy γ for different levels of uniaxial stress σ_0 (100, 200, and 300 MPa).

From the diagram, it can be seen that with increasing uniaxial stress, the curve shifts downward, indicating that the system becomes unstable at lower surface energies. This suggests that higher stresses promote the onset of instability. For a given uniaxial stress, as the surface energy increases, the critical wave number q_c also increases. This implies that higher surface energies tend to stabilize the system against the ATG instability. The area below each curve represents stable configurations for the given stress level, while the area above each curve indicates conditions under which the system is likely to become unstable.

III. RESULTS AND DISCUSSION

In this work, a phase-field model is proposed to calculate the ATG instability in the Allen–Cahn framework.

A. Morphological evolution

The computational domain is $100 \times 50 \times 1$, the time steps are 20000, and the t -step is 0.05. The boundary conditions for the thin film are set as follows: Periodic boundary conditions apply to the left and right boundaries, while the top and bottom boundaries are isolated. The phi index is shown in Fig. 3. In the initial stage, the interface is flat, as shown in Fig. 3(a). Over time, the thin film continues to grow and becomes thicker, as shown in Fig. 3(b). At time $t = 25$, the interface begins to appear as an unstable perturbation phenomenon, as shown in Fig. 3(c). The perturbation becomes increasingly stronger, as can be seen in Figs. 3(d) and 3(e), and leads to a misfit dislocation, as shown in Fig. 3(f). As time progress, the misfit becomes larger, as can be seen in Fig. 3(g). Figure 3(h) shows that the height continues to grow. From the simulation, it can be seen that the critical thickness is 5.08 nm.

B. Evolution of elastic stress

The von Mises distribution is shown in Fig. 4.

At the beginning, the stress is quite low, as shown in Fig. 4(a). As the driving force is applied, the stress increases, as can be seen in Figs. 4(b)–4(e), with the maximum stress occurring at the bottom of the thin film. There is also a gradual accumulation of energy. When this accumulation reaches a certain level, there is a mismatch in the interface. Following this, the energy relaxes, as shown in Fig. 4(f). After the occurrence of the misfit, the stress is quite low, as shown in Figs. 4(g) and 4(h).

The temporal variation in the maximum stress is shown in Fig. 5. In the initial phase, the maximum stress increases gradually. When the stress is large enough, dislocations occur in the thin film. Then the stress decreases drastically. After dropping to a certain level, it gradually becomes stable.

C. Effect of surface energy

To study the influence of surface energy on the morphology, different values of surface energy (G_{ab}) are set: 0, 0.01, 0.02, 0.03, 0.04, 0.05, 0.06, 0.07, 0.08, 0.09, and 0.1. The maximum stress at different surface energies (G_{ab}) is shown in Fig. 6.

Figure 6 shows that the maximum stress continues to increase in the initial phase when the value of the surface energy (G_{ab}) is 0 but then remains stable for a longer period of time and does not grow any further. If the value of the surface energy (G_{ab}) is equal to 0, a breakup does not occur. When the value of the surface energy (G_{ab}) varies from 0.01 to 0.1, the trend of change in the maximum stress is consistent. The maximum stress increases gradually. To a certain extent, the breakup occurs and the stress decreases sharply. If the value of the surface energy (G_{ab}) is higher, the breakup occurs faster. Figure 6 shows that the breakup occurs earliest when the value of the surface energy (G_{ab}) is equal to 0.1. When the value of the surface energy (G_{ab}) is equal to 0.01, the breakup occurs the latest.

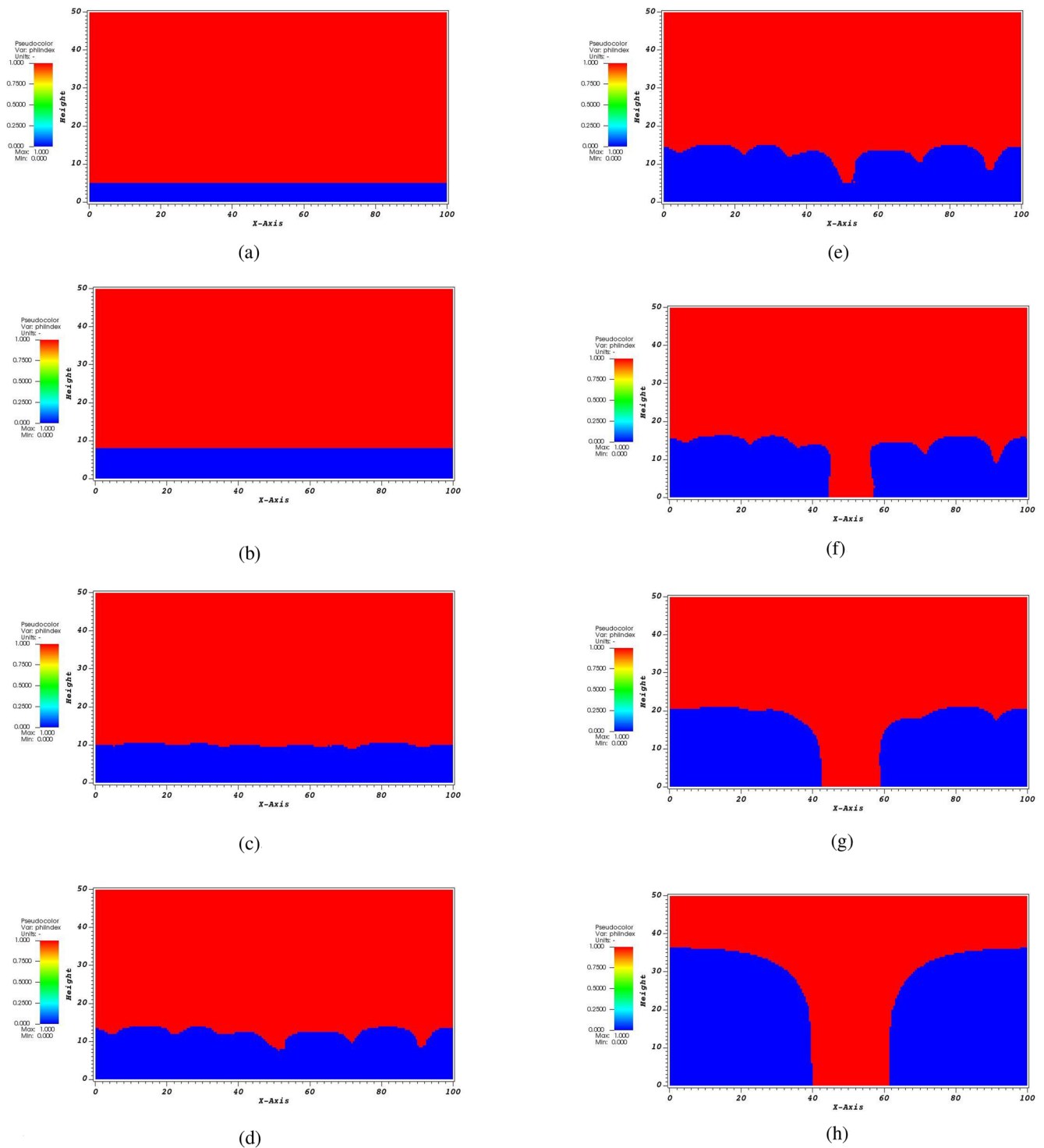


FIG. 3. Morphology at different times. (a) Time=0, initial stage of the thin film, showing a flat interface. (b) Time=150, growth phase of the thin film, with increased thickness. (c) Time=250, onset of instability, beginning of surface perturbations. (d) Time=350, progression of instability, with more pronounced perturbations. (e) Time=375, advanced stage of instability, leading to significant undulations. (f) Time=400, formation of misfit dislocations, due to increased stress. (g) Time=500, further development of misfit, with larger undulations. (h) Time=1000, advanced growth stage, showing a continued increase in height and complexity of the surface morphology.

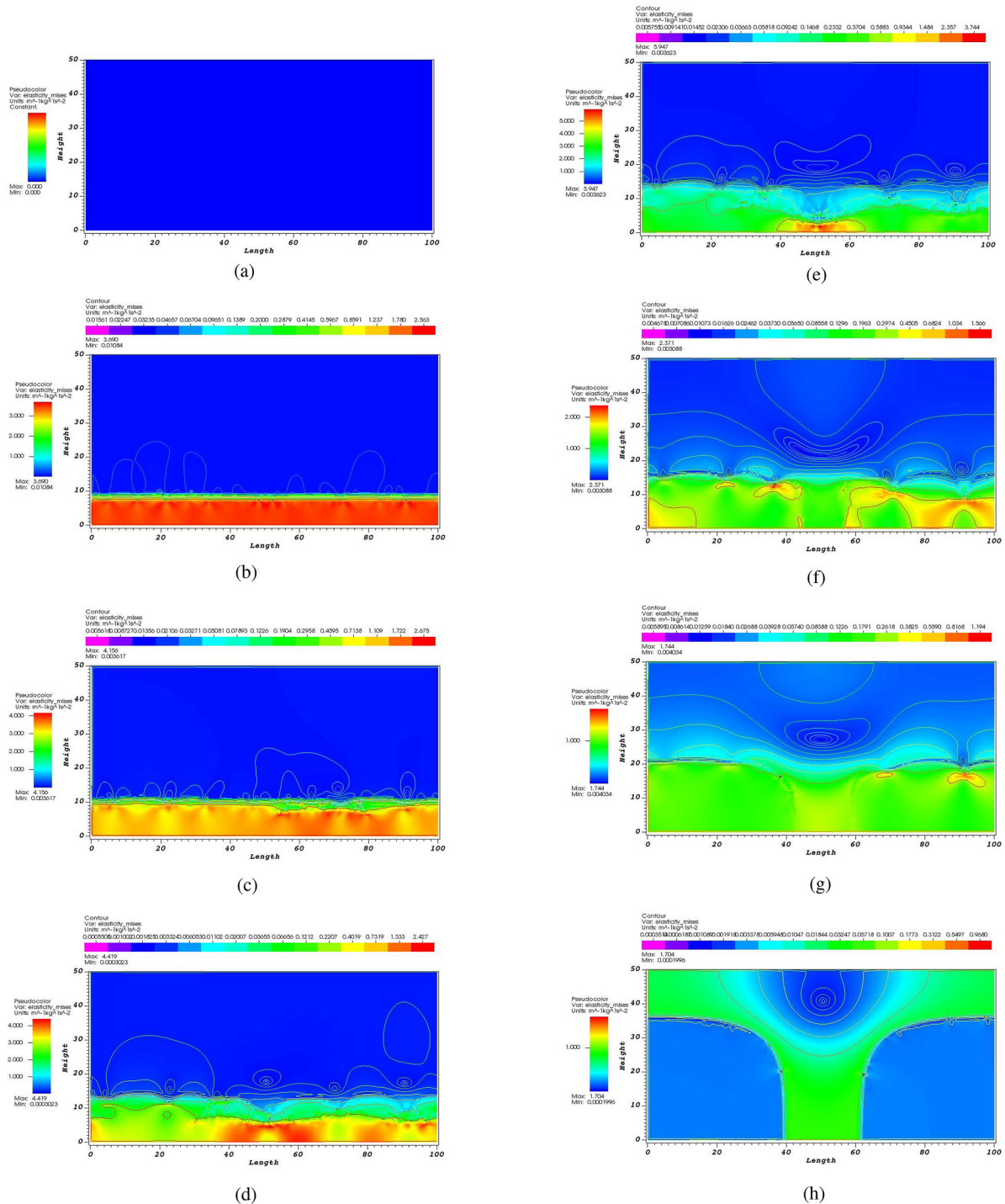


FIG. 4. von Mises distribution at different times. (a) Time=0, initial elastic stress distribution in the film, indicating low stress levels. (b) Time=150, increased stress distribution, as the film grows. (c) Time=250, the stress distribution intensifies, signifying the onset of surface perturbations. (d) Time=350, the stress distribution becomes more heterogeneous and there is surface perturbations. (e) Time=375, the surface perturbations intensify due to increasing elastic energy. (f) Time=400, the formation of misfit dislocations is observed, resulting from the accumulated stress exceeding the elastic limit of the film material. (g) Time=500, the development of misfit is further highlighted, with larger undulations and stress concentration, particularly at the bottom of the thin film. (h) Time=1000, the advanced growth stage is reached, characterized by the continued increase in height and complexity of surface morphology along with the associated stress distribution.

17 April 2024 10:44:32

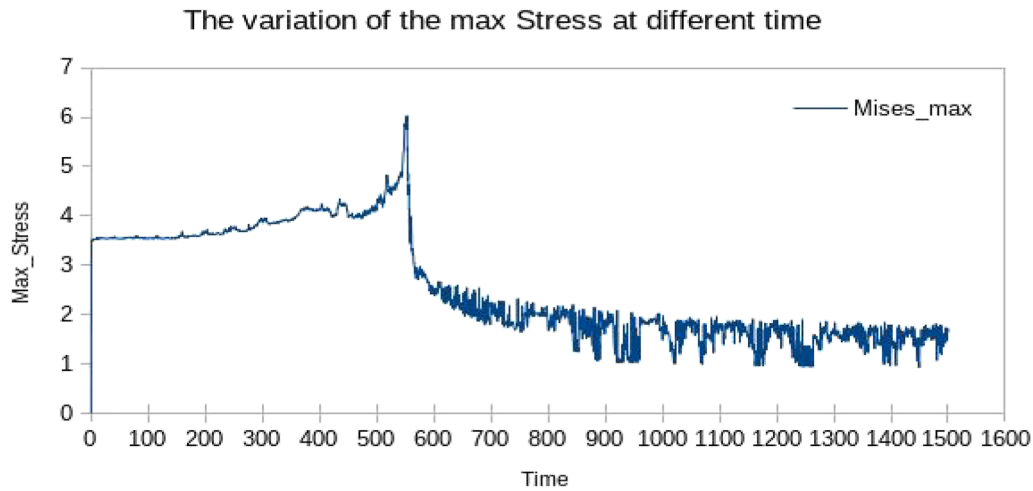


FIG. 5. Graph showing the variation in the maximum von Mises stress in the film over time. The graph illustrates an initial gradual increase in stress, followed by a sharp decrease corresponding to the occurrence of dislocations, and finally a stabilization of stress levels.

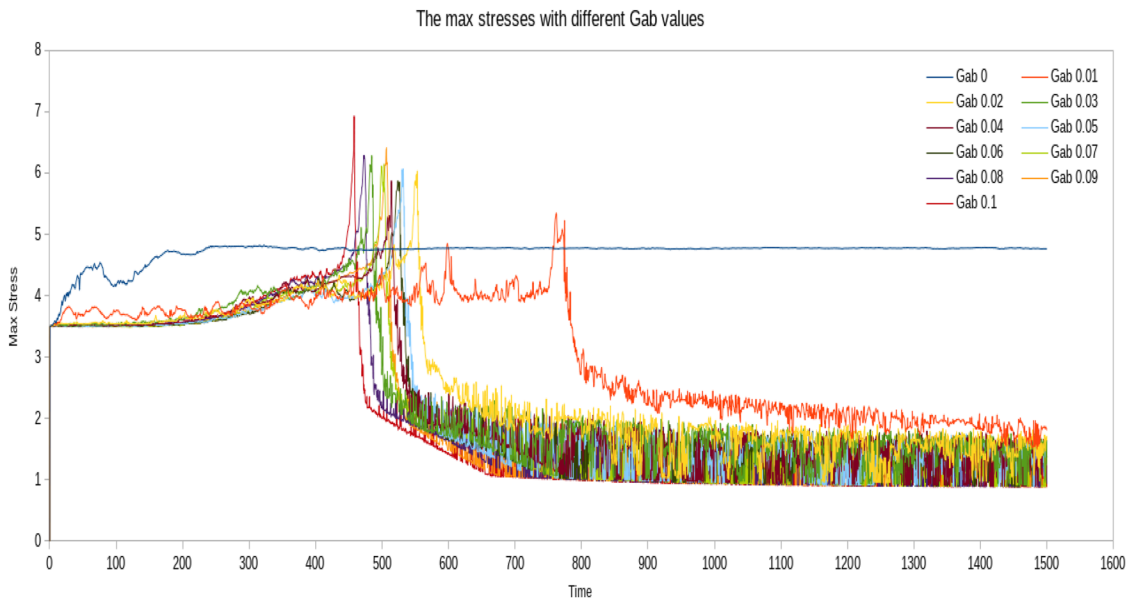


FIG. 6. Comparative graph of maximum stress levels at different surface energy values G_{ab} . Each curve represents a different G_{ab} value, highlighting the impact of surface energy on the stress behavior and the timing of instability and breakup in the film.

For the different surface energy values G_{ab} , the instability and fracture times are different, as shown in Fig. 7. When the surface energy G_{ab} is equal to 0.01, the unstable and fracture times are 325.5 and 762, respectively. While the surface energy G_{ab} is equal to 0.1, the unstable and fracture times are 226.5 and 458, respectively. From Fig. 7, it can be seen that the larger the value of G_{ab} , the sooner the instability and breakup occur.

The unstable stress and the fracture stress at different values of the surface energy (G_{ab}) are shown in Fig. 8. When the surface energy (G_{ab}) is equal to 0.01, the unstable and fracture stresses are

3.85 and 5.34, respectively. While the surface energy (G_{ab}) is 0.1, the unstable and fracture stresses are 3.59 and 6.93, respectively. From Fig. 8, it can be seen that the maximum fracture stress increases with the increase in the surface energy value (G_{ab}). The larger the value of G_{ab} , the greater the breakup stress. In the case of unstable stresses, the changes in stress values at different surface energies (G_{ab}) are not obvious.

The critical thickness and the fracture thickness at different surface energies (G_{ab}) are shown in Fig. 9. With increasing surface energy (G_{ab}), the fracture thickness gradually decreases. Due to

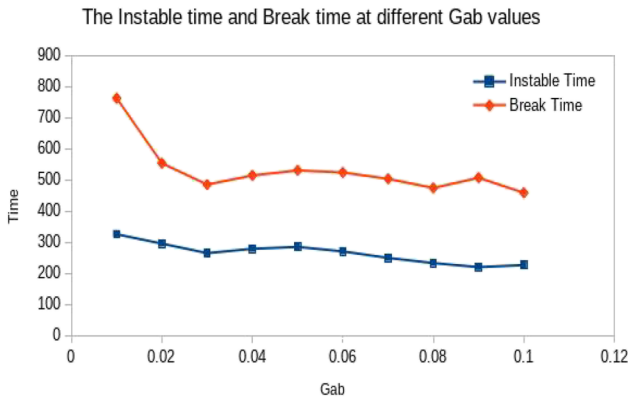


FIG. 7. Bar chart showing the variation in the instability and fracture times for different surface energy (G_{ab}) values. The chart compares the onset times of instability and the occurrence of fracture across a range of G_{ab} values.

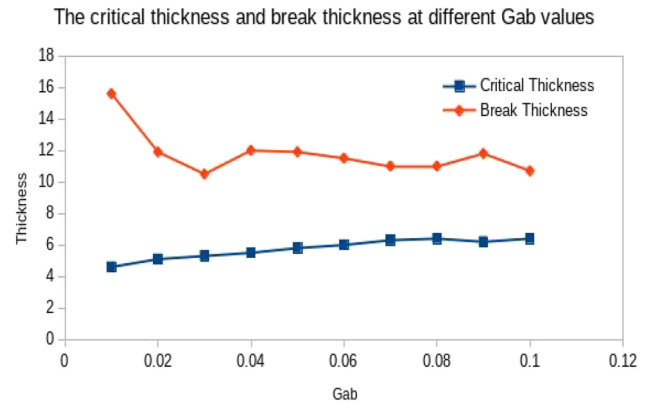


FIG. 9. Comparison of critical and fracture thicknesses at different surface energy (G_{ab}) values. The plot reveals a decreasing trend in fracture thickness and an increasing trend in critical thickness as G_{ab} values increase.

assumptions and random settings, the fracture thickness at a given node is not strictly reduced, but it is reasonable. However, the general trend of change in fracture thickness decreases with the increase in surface energy (G_{ab}), while the critical thickness grows as the surface energy (G_{ab}) increases. This shows that the critical thickness is affected by the surface energy (G_{ab}).

D. Benchmarking tests and validation

To provide benchmark results for the Asaro–Tiller–Grinfeld (ATG) instability, we need to focus on the numerical simulations performed using the phase-field model. In the epitaxy of strained layers, there is a mismatch between the atoms on either side of the interface. The lattice misfit (or misfit strain) f can be expressed in simplified terms as³¹

$$f = \frac{a_s - a_f}{a_f}, \quad (31)$$

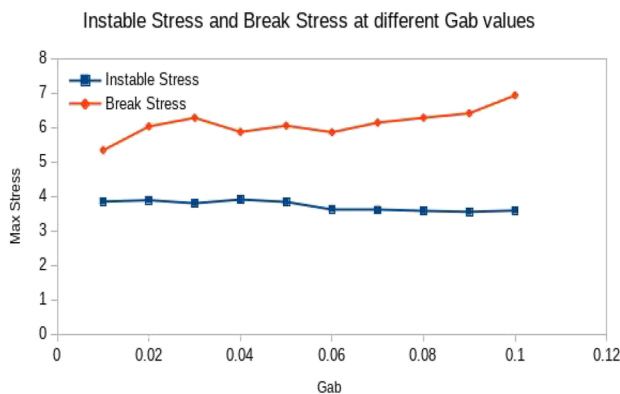


FIG. 8. Analysis of unstable and breakup stress levels at various G_{ab} values. This figure illustrates how the maximum breakup stress increases with higher G_{ab} values, whereas the change in unstable stress is less pronounced across different surface energies.

where a_f and a_s are the lattice parameters of the thin film and the substrate, respectively. Compared to the unrelaxed state, the energy can be reduced by two mechanisms: (a) generation of interfacial dislocations and (b) compression or expansion that reduces the difference between the lattice parameters. Defect-free growth is possible when the parabolic strain energy is less than the interfacial energy.⁴ With some approximations, dislocation-free growth can be achieved for thicknesses below a critical thickness. In this study, according to the empirical formula obtained from the experiment, the critical thickness h_c can be expressed as

$$h_c = \frac{b}{2\pi f} \frac{(1 - \nu \cos^2 \alpha)}{(1 + \nu) \cos \beta} \left(\ln \frac{h_c}{b} + 1 \right), \quad (32)$$

where b is the strength of the dislocations, α is the angle between the dislocation line and its Burgers vector, β is the angle between the slip direction and the direction in the film plane that is perpendicular to the intersection of the slip plane and the interface, and ν is Poisson’s ratio. For the material InAs, using the same process parameters as those given in Sec. III A, the critical thickness h_c is about 5.26 nm.

The critical thickness given by Eq. (32) is true for an infinite substrate and would actually represent a lower limit when the strain is shared by a substrate of finite thickness, as in a strained layer super lattice. The critical thicknesses are a little higher than those calculated theoretically and attributed the difference to diffusion effects.

These results will validate the model’s capability in accurately simulating the ATG instability in thin films under various conditions:

Simulation Setup and Parameters

Model Parameters: Based on the provided material properties of InAs and equations outlined in the article. Simulation Domain: Set as $100 \times 50 \times 1$, with a spatial discretization of $\Delta x = \Delta y = \Delta z = 0.5$. Time Steps: 20 000, with a t-step of 0.05. Boundary Conditions: Periodic conditions on the left and right boundaries; top and bottom boundaries are isolated.

Morphological Evolution and Stress Distribution

Initial Stage: Examined the initial flat interface and its evolution over time. Growth Phase: Monitored the growth and increased thickness of the thin film. Instability Onset: Observed the formation of unstable perturbations and the subsequent development of misfit dislocations. Stress Analysis: Tracked the distribution of von Mises stress, noting the peak stress locations and the relaxation after misfit occurrence.

Effect of Surface Energy on Instability

Variable Surface Energy: Tested with varying surface energy (G_{ab}) values ranging from 0 to 0.1. Observations: Noted the impact of different G_{ab} values on the time of instability onset, maximum stress, and breakup behavior.

Critical and Fracture Thickness Analysis

Thickness Measurements: Determined the critical and fracture thicknesses under varying surface energy conditions. Comparison with Theoretical Predictions: Validated the simulated critical thickness against theoretical predictions.

Stability Analysis

Stability Diagram: Created to demonstrate the relationship between critical wave number (q_c), surface energy (γ), and uniaxial stress (σ_0).

From the observations, the critical thickness of the thin film was found to be 5.08 nm, aligning closely with theoretical predictions. Higher surface energy values led to an earlier onset of instability and breakup in the film. The maximum fracture stress increased with increasing surface energy, while the unstable stress showed less variation. A decreasing trend in fracture thickness with increasing surface energy was observed. The stability diagram underscored the impact of uniaxial stress and surface energy on the ATG instability.

The benchmarks highlighted the model's effectiveness in simulating morphological evolution, stress distribution, and the influence of key material and environmental parameters. This comprehensive analysis provides a solid foundation for understanding and predicting the behavior of thin films under mechanical stress, contributing significantly to the field of materials science and surface engineering.

IV. CONCLUSION

To investigate the ATG instability in the Allen–Cahn framework, a two-dimensional mathematical model is created in the software PACE3D.

We present a phase field model of Asaro–Tiller–Grinfeld (ATG) instability driven by surface diffusion. The surface corrugation of the elastically strained film was numerically simulated in two dimensions. The model includes the elastic strain field generated by the non-hydrostatic stress, and using the local mechanical equilibrium condition, the displacement field is obtained as a function of the order parameter. We perform the fitted asymptotic expansion analysis and show that our phase field model reduces to the sharp interface model of the Asaro–Tiller–Grinfeld instability in the sharp interface limit. By performing a two-dimensional numerical stability analysis, it is proven that the model represents the instability of an elastically stressed surface well.

- Initially, the thickness of the thin film increases with time. When it reaches a critical value, the thin film starts to become unstable. The critical thickness of the thin film is 5.08 nm.
- The interface breaks into several parts due to the elastic stresses, but no breakup occurs if the surface energy (G_{ab}) is equal to 0.
- The larger the surface energy, the sooner the instability and breakup occur.
- The maximum fracture stress increases with an increase in surface energy (G_{ab}), while the surface energy (G_{ab}) has little effect on the unstable stress.
- The fracture thickness decreases with increasing surface energy (G_{ab}), while the critical thickness increases with the increase in the surface energy (G_{ab}).

ACKNOWLEDGMENTS

This work was financially supported by the China and Germany Postdoctoral Exchange Program 2020 from the Office of China Postdoctoral Council and the Helmholtz Center, Postdoctoral Research Foundation of China (China Postdoctoral Research Foundation), Grant No. ZD2020026. This work was also supported by the China Postdoctoral Science Foundation (China Postdoctoral Foundation Project), Grant No. 2019M650658. The authors are grateful for all contributors of the PACE3D framework.

AUTHOR DECLARATIONS

Conflict of Interest

The authors have no conflicts to disclose.

Author Contributions

Xuyang Chen: Conceptualization (equal); Data curation (equal); Formal analysis (equal); Funding acquisition (equal); Investigation (equal); Methodology (equal); Project administration (equal); Software (equal); Validation (equal); Writing – original draft (equal); Writing – review & editing (equal). **Guangchao Li:** Conceptualization (equal); Data curation (equal); Formal analysis (equal); Funding acquisition (equal); Investigation (equal); Methodology (equal); Project administration (equal); Software (equal); Validation (equal); Writing – original draft (equal); Writing – review & editing (equal). **Feng Lin:** Conceptualization (supporting); Data curation (supporting); Formal analysis (supporting); Funding acquisition (lead); Investigation (equal); Project administration (lead); Validation (lead); Visualization (equal).

DATA AVAILABILITY

The data that support the findings of this study are available from the corresponding author upon reasonable request.

REFERENCES

- W. P. McCray, “MBE deserves a place in the history books,” *Nat. Nanotechnol.* **2**, 259–261 (2007).
- A. Danescu, “The Asaro–Tiller–Grinfeld instability revisited,” *Int. J. Solids Struct.* **38**, 4671–4684 (2001).

- ³R. Asaro and W. Tiller, "Interface morphology development during stress corrosion cracking: Part I. Via surface diffusion," *Metall. Trans.* **3**, 1789–1796 (1972).
- ⁴J. H. Van Der Merwe, "Crystal interfaces. Part I. Semi-infinite crystals," *J. Appl. Phys.* **34**, 117–122 (1963).
- ⁵A. Krost, C. Berger, P. Moser, J. Bläsing, A. Dadgar, C. Hums, T. Hempel, B. Bastek, P. Veit, and J. Christen, "Stranski–Krastanov transition and self-organized structures in low-strained AlInN/GaN multilayer structures," *Semicond. Sci. Technol.* **26**, 014041 (2010).
- ⁶K. Kassner and C. Misbah, "A phase-field approach for stress-induced instabilities," *Europhys. Lett.* **46**, 217 (1999).
- ⁷Y. Ren, L. Liwang, L. Liang, Q. Zheng, Y. Xu, L. Zhang, and W.-F. Rao, "Influences of the substrate strain on microstructures of L10 FePt-X thin films by using phase field simulation," *Mat. Today Commun.* **32**, 104123 (2022).
- ⁸M. W. Liu, M. P. Gururajan, and K.-A. Wu, "Morphological evolution of grain boundaries under lateral strains," *Phys. Rev. Mater.* **6**(2), 023601 (2022).
- ⁹K. Kassner, C. Misbah, J. Müller, J. Kappey, and P. Kohlert, "Phase-field modeling of stress-induced instabilities," *Phys. Rev. E* **63**, 036117 (2001).
- ¹⁰Z.-F. Huang and R. C. Desai, "Stress-driven instability in growing multilayer films," *Phys. Rev. B* **67**, 075416 (2003).
- ¹¹D.-H. Yeon, P.-R. Cha, and M. Grant, "Phase field model of stress-induced surface instabilities: Surface diffusion," *Acta Mater.* **54**, 1623–1630 (2006).
- ¹²B. Chirranjeevi, T. Abinandanan, and M. Gururajan, "A phase field study of morphological instabilities in multilayer thin films," *Acta Mater.* **57**, 1060–1067 (2009).
- ¹³M. A. Zaeem and S. D. Mesarovic, "Morphological instabilities in thin films: Evolution maps," *Comput. Mater. Sci.* **50**, 1030–1036 (2011).
- ¹⁴C. Köhler, R. Backofen, and A. Voigt, "Relaxation of curvature-induced elastic stress by the Asaro–Tiller–Grinfeld instability," *Europhys. Lett.* **111**, 48006 (2015).
- ¹⁵Y. Zhang and M. Tang, "Stress-induced intercalation instability," *Acta Mater.* **201**, 158–166 (2020).
- ¹⁶D. Schneider, O. Tschukin, A. Choudhury, M. Selzer, T. Böhlke, and B. Nestler, "Phase-field elasticity model based on mechanical jump conditions," *Comput. Mech.* **55**, 887–901 (2015).
- ¹⁷D. Schneider, E. Schoof, O. Tschukin, A. Reiter, C. Herrmann, F. Schwab, M. Selzer, and B. Nestler, "Small strain multiphase-field model accounting for configurational forces and mechanical jump conditions," *Comput. Mech.* **61**, 277–295 (2018).
- ¹⁸B. Nestler, F. Wendler, M. Selzer, B. Stinner, and H. Garcke, "Phase-field model for multiphase systems with preserved volume fractions," *Phys. Rev. E* **78**, 011604 (2008).
- ¹⁹P. G. Kubendran Amos, L. T. Mushongera, and B. Nestler, "Phase-field analysis of volume-diffusion controlled shape-instabilities in metallic systems-I: 2-Dimensional plate-like structures," *Comput. Mater. Sci.* **144**, 363–373 (2018).
- ²⁰P. G. Kubendran Amos, E. Schoof, J. Santoki, D. Schneider, and B. Nestler, "Limitations of preserving volume in Allen–Cahn framework for microstructural analysis," *Comput. Mater. Sci.* **173**, 109388 (2020).
- ²¹M. S. McCallum, P. W. Voorhees, M. J. Miksis, S. H. Davis, and H. Wong, "Capillary instabilities in solid thin films: Lines," *J. Appl. Phys.* **79**, 7604–7611 (1996).
- ²²M. P. Gururajan and A. Lahiri, "Elastic stress effects on microstructural instabilities," [arXiv:1607.00599](https://arxiv.org/abs/1607.00599) (2016).
- ²³A. Rätz, A. Ribalta, and A. Voigt, "Surface evolution of elastically stressed films under deposition by a diffuse interface model," *J. Comput. Phys.* **214**, 187–208 (2006).
- ²⁴B. Nestler, H. Garcke, and B. Stinner, "Multicomponent alloy solidification: Phase-field modeling and simulations," *Phys. Rev. E* **71**, 041609 (2005).
- ²⁵A. Choudhury and B. Nestler, "Grand-potential formulation for multicomponent phase transformations combined with thin-interface asymptotics of the double-obstacle potential," *Phys. Rev. E* **85**, 021602 (2012).
- ²⁶C. Herrmann, E. Schoof, D. Schneider, F. Schwab, A. Reiter, M. Selzer, and B. Nestler, "Multiphase-field model of small strain elasto-plasticity according to the mechanical jump conditions," *Comput. Mech.* **62**, 1399–1412 (2018).
- ²⁷N. Moelans, "A quantitative and thermodynamically consistent phase-field interpolation function for multi-phase systems," *Acta Mater.* **59**, 1077–1086 (2011).
- ²⁸D. Schneider, F. Schwab, E. Schoof, A. Reiter, C. Herrmann, M. Selzer, T. Böhlke, and B. Nestler, "On the stress calculation within phase-field approaches: A model for finite deformations," *Comput. Mech.* **60**, 203–217 (2017).
- ²⁹I. Steinbach and F. Pezzolla, "A generalized field method for multiphase transformations using interface fields," *Physica D* **134**, 385–393 (1999).
- ³⁰M. Silhavy, *The Mechanics and Thermodynamics of Continuous Media* (Springer Science & Business Media, 2013).
- ³¹R. Folch and M. Plapp, "Quantitative phase-field modeling of two-phase growth," *Phys. Rev. E* **72**, 011602 (2005).
- ³²P. K. Bhattacharya, U. Das, F.-Y. Juang, Y. Nashimoto, and S. Dhar, "Material properties and optical guiding in InGaAs-GaAs strained layer superlattices—A brief review," *Solid-State Electron.* **29**, 261–267 (1986).
- ³³K. Nakajima, T. Ujihara, G. Sazaki, and N. Usami, "Phase diagram calculation for epitaxial growth of GaInAs on InP considering the surface, interfacial and strain energies," *J. Cryst. Growth* **220**, 413–424 (2000).
- ³⁴S. Korte, I. Farrer, and W. Clegg, "Elastic and plastic properties of $\text{In}_x\text{Ga}_{1-x}\text{As}$," *J. Phys. D: Appl. Phys.* **41**, 205406 (2008).
- ³⁵G. I. Tóth, T. Pusztai, and L. Gránásy, "Consistent multiphase-field theory for interface driven multidomain dynamics," *Phys. Rev. B* **92**, 184105 (2015).